

Optical Information Multiplexing with Nonlinear Coding Metasurfaces

Menglin Ma, Zhi Li, Wenwei Liu, Chengchun Tang, Zhancheng Li, Hua Cheng, Junjie Li, Shuqi Chen,* and Jianguo Tian

Coding metasurfaces, as a new type of design concept, have provided many attractive functionalities for manipulating the wave fronts of light. Previous research only focused on linear coding metasurfaces; however, with the increasing demand for highly integrated and compact multifunctional chips, the drawbacks of linear coding metasurfaces, the constraints on information capacity and operating frequency are becoming more and more obvious. Here, Pancharatnam–Berry-phase-based nonlinear coding metasurfaces are proposed, in which convenient digital signal processing is employed to design multidimensional information channels in nonlinear optical processes to achieve optical information multiplexing. In order to confirm the feasibility of this methodology, by encoding various focusing functionalities and image information into nonlinear metasurfaces, a multifocal metalens and a multifunctional metasurface are theoretically designed, and their excellent performances are experimentally demonstrated. The proposed nonlinear coding metasurfaces may provide a promising platform for information encryption, multi-channel optical data storage, and real space encoding imaging.

their excellent abilities to manipulate the amplitude, phase, and polarization of electromagnetic waves. A series of attractive phenomena have been introduced by metamaterials, including negative refractive index,^[1–4] super-imaging,^[5–7] and invisibility cloaking.^[8–11] Recently, metasurfaces, as the promising 2D equivalents of metamaterials, have been rapidly developed due to their relatively smaller difficulty of fabrication and lower optical loss compared with bulk metamaterials. By controlling the shape, size, and orientation of each meta-atom, metasurfaces can arbitrarily manipulate the wave fronts of light at the sub-wavelength scale to achieve different functionalities. In particular, by changing the orientation angle of meta-atom, different Pancharatnam–Berry (P–B) phase information can be conveniently stored in it. P–B metasurfaces, which consist of meta-atom arrays with carefully designed orientation

1. Introduction

Metamaterials, which consist of artificial sub-wavelength meta-atoms, have been widely concerned and studied, owing to


angles, have demonstrated a lot of fascinating properties, such as holography,^[12–15] Fourier transformation,^[16] anomalous refraction or reflection,^[17–23] vortex or vector beam generating,^[17,24–27] photonic spin Hall effect,^[28–32] and so on. However, most of the metasurfaces have only a single operating frequency and small information capacity, which are not enough to meet the increasing demand for highly integrated and compact multifunctional devices. In this case, the research and exploitation of nonlinear optical responses of metasurfaces become very necessary because it can introduce multidimensional information storage channels originating from light-frequency conversion processes, which are very beneficial to realizing optical data multiplexing and enlarging the information capacity.

Dr. M. L. Ma, Dr. Z. Li, Dr. W. W. Liu, Dr. Z. C. Li, Prof. H. Cheng,
Prof. S. Q. Chen, Prof. J. G. Tian
The Key Laboratory of Weak Light Nonlinear Photonics
Ministry of Education
School of Physics and TEDA Institute of Applied Physics
Nankai University
Tianjin 300071, China
E-mail: schen@nankai.edu.cn

Dr. C. C. Tang, Prof. J. J. Li
Beijing National Laboratory for Condensed Matter Physics
Institute of Physics, Chinese Academy of Sciences
P.O. Box 603, Beijing 100190, China

Prof. S. Q. Chen
The collaborative Innovation Center of Extreme Optics
Shanxi University
Taiyuan, Shanxi 030006, China

Prof. S. Q. Chen, Prof. J. G. Tian
Renewable Energy Conversion and Storage Center
Nankai University
Tianjin 300071, China

 The ORCID identification number(s) for the author(s) of this article can be found under <https://doi.org/10.1002/lpor.201900045>

DOI: 10.1002/lpor.201900045

In information science, digital signal processing (DSP) based on conventional electric signals is serial, but DSP based on optical signals is parallelizable, which provides the high information density and fast processing speed. Since the first report by Cui et al.,^[33] as an alternative research approach, coding metasurfaces have caught much attention due to the convenient DSP.^[34] Coding metasurfaces take the mechanism that uses digital elements to characterize the phases of meta-atoms.^[33] In other words, the digital elements of 1-bit coding metasurfaces are “0” and “1,” which can be realized by designing meta-atoms with the phases 0 and π , respectively. The digital elements of 2-bit coding metasurfaces are composed of “00,” “01,” “10” and “11,” which can

be realized by engineering meta-atoms with the phases 0 , $\pi/2$, π , and $3\pi/2$, respectively. Similarly, the phases corresponding to the digital elements of n -bit coding metasurfaces can be obtained by dividing the phase 2π by 2^n . Therefore, as the bridge between physical metasurface particles and digital codes, coding metasurfaces can realize many exotic phenomena more simply and effectively through the way of DSP, such as diffuse scattering, vortex beam, and beam bending. It is worth mentioning that the application scope of coding metasurfaces is not only limited to electromagnetic waves^[35–37] but also has extended to acoustic waves.^[38–40]

The incorporation of nonlinear responses into coding metasurfaces, that is, performing DSP on the design of multi-frequency channels, has great superiority to achieve highly integrated and multifunctional devices. Previously, by utilizing linear and nonlinear optical processes, Ye et al. obtained multi-channel information capacity within a single nonlinear metasurface.^[41] After that, the nonlinear P–B metasurface proposed by Walter et al. stored the optical information into SHG signal by the way of real space image encoding, which opened new avenues for securing optical information.^[42] Recently, by introducing nonlinear P–B phases, Li et al. achieved threefold capacity of optical vortices with different topological charges using an ultrathin nonlinear metasurface, which represents a new strategy for multi-channel optical manipulation and information security.^[43] However, to the best of our knowledge, in addition to the multi-dimensional information capacity and real space image coding, there have been no further explorations in the research field of nonlinear coding metasurfaces, especially the further combination of digital coding elements in information science and third harmonic generation (THG) in nonlinear optics. On the basis of the previous works, the introduction of digital coding will provide a more flexible and concise strategy for the design of multi-dimensional information storage.

Here, we propose the PB-phase-based nonlinear coding metasurfaces, which consist of the arrays of split-ring resonators (SRRs) with spatially varying orientations. By selecting eight meta-atoms with predesigned orientation angles as coding elements, nonlinear coding metasurfaces can realize 1-bit, 2-bit, and 3-bit coding at the THG, fundamental frequency (FF), and second harmonic generation (SHG), respectively. As examples, we encoded the nonlinear multifocal metalens and nonlinear multifunctional metasurface, the excellently multiplexed performances of which are demonstrated by both numerical calculations and experiments. Therefore, the nonlinear coding metasurfaces, as the bridge between physical nonlinear metasurfaces and digital codes, which make the manipulation of information channels more flexible and convenient, provide a promising platform for many fascinating applications such as information encryption, optical information multiplexing, and multi-channel optical data storage.

2. Results and Discussion

We choose the SRRs with one-fold rotational symmetry as the building blocks of nonlinear coding metasurfaces since they support magnetic resonance modes and can simultaneously manipulate the wave fronts of THG, FF, and SHG to implement 1-bit

to 3-bit coding (see Table S1, Supporting Information). As an effective control method of local phase shifts, P–B phase is associated with space-variant polarization manipulation, which can achieve continuous phase control in complete range (0 – 2π). As shown schematically in Figure 1a, a circularly polarized beam with spin state σ is applied as incident source at FF, where $\sigma = \pm 1$ represents left-hand circularly polarized (LCP) or right-hand circularly polarized (RCP) light, respectively. In the linear optical regime, when the fundamental beam with spin state σ is incident onto the SRR with the orientation angle of φ , due to the anisotropic response of SRR, the spin state of incident beam will be flipped upon interaction with meta-atom, which will generate a P–B phase of $2\sigma\varphi$ for the transmitted beam with spin state $-\sigma$. Owing to the lack of rotational symmetry of the SRRs, the SHG and THG of both spin states can be simultaneously generated in the nonlinear optical regime. In the case of the n th harmonic generation, nonlinear P–B phases $(n \pm 1)\sigma\varphi$ are obtained, where ± 1 stands for the opposite or same spin state of harmonic generation compared to that of the fundamental beam.^[44] Therefore, the nonlinear P–B phases of the SHG with spin σ and $-\sigma$ are $\sigma\varphi$ and $3\sigma\varphi$, respectively. The P–B phases of the THG with spin σ and $-\sigma$ are $2\sigma\varphi$ and $4\sigma\varphi$, respectively. In order to more perfectly combine the concepts of nonlinearity and coding, the THG with spin $-\sigma$, FF with spin $-\sigma$, and SHG with spin σ are selected as the three channels to realize optical information multiplexing.

For these three certain information storage channels of THG, FF, and SHG from the same metasurface, the corresponding P–B phases are 4φ , 2φ , and φ in the case of LCP incident light, respectively. We can find two rules from these phases, which can be used to implement the process of digital coding. First, the P–B phase of SHG is equal to the orientation angle of meta-atom, which is one-half of the P–B phase of FF and one-fourth of the P–B phase of THG. In order to determine the orientation angle distributions of SRRs in nonlinear coding metasurfaces, we only need to know the phase distributions of SHG. For the purpose of applying DSP to design nonlinear metasurface, the eight meta-atoms with orientation angles 0 , $\pi/4$, $\pi/2$, $3\pi/4$, π , $5\pi/4$, $3\pi/2$, and $7\pi/4$ are selected, as listed in Table 1. For these meta-atoms, the P–B phases of THG are easily obtained, which consist of four sets of the phases 0 and π in the range of 0 – 2π , and can be encoded with 1-bit digital elements, that is, 0 –“0,” π –“1.” According to the orientation angles of eight meta-atoms, the P–B phases of FF are composed of two groups of 0 , $\pi/2$, π , and $3\pi/2$ which can be encoded with 2-bit digital elements. Similarly, the nonlinear P–B phases of SHG can be encoded with 2-bit coding elements. Second, for the same meta-atom, there is an extra degree of freedom arising from the fact that the digital elements “0” of THG correspond to the “00” and “10” of FF at the same time, and the digital elements “00” of FF correspond to digital elements “000” and “100” of SHG. It is worth noting that this extra degree of freedom is unidirectional because the coding elements “000” of SHG can only correspond to the “00” of FF, and the coding elements “00” of FF can only correspond to the “0” of THG. So we can relatively independently design these channels by the extra degree of freedom from THG to FF to SHG. This extra degree of freedom reduces the correlation among the three information storage channels, which provides an effective way for the relatively independent design of real space imaging of multifunctional metasurface under different channels.

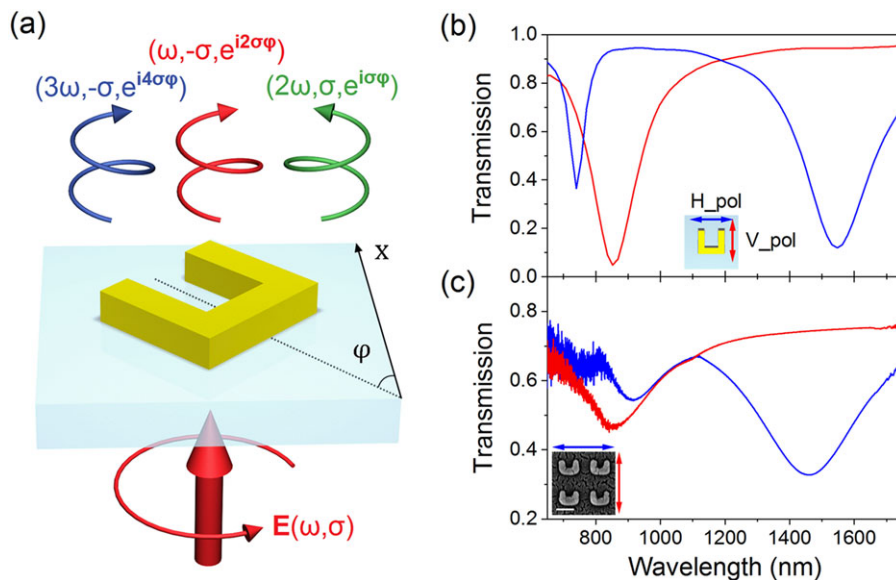


Figure 1. Schematic diagram of the P–B phases and the linear optical properties of the sample consisting of regularly arranged SRRs. a) Schematic diagram of the linear and nonlinear P–B phases. For a SRR with the orientation angle of φ under the incident circularly polarized fundamental beam with spin state σ , the P–B phases are 4φ , 2φ , and φ for THG with cross-circular polarization (CP), FF with cross-CP and SHG with co-CP, respectively. The designed SRR has a length of 168 nm, a width of 150 nm, a height of 35 nm, and an arm width of 40 nm. The period between the meta-atoms is 350 nm in both directions. b) Simulated linear transmission spectra for horizontal and vertical polarized incident lights of the regularly arranged SRRs. The fundamental plasmonic mode is around the wavelength of 1550 nm (the center wavelength of femtosecond laser). c) Measured transmission spectra for horizontal and vertical polarized incident lights of the regularly arranged SRRs. The resonance dip of the first-order mode is around the wavelength of 1460 nm. The inset shows the SEM image of the sample with regularly arranged SRRs. The scale bar is 200 nm.

Table 1. The DSP for the P–B phases of meta-atoms with predesigned orientation angles.

n-bit	Harmonic generation	Digital coding for the P–B phases of meta-atoms with predesigned orientation angles							
		0	$\pi/4$	$\pi/2$	$3\pi/4$	π	$5\pi/4$	$3\pi/2$	$7\pi/4$
1-bit	THG	0	1	0	1	0	1	0	1
2-bit	FF	00	01	10	11	00	01	10	11
3-bit	SHG	000	001	010	011	100	101	110	111

In order to boost nonlinear conversion efficiency, the approach of 3D finite-difference time-domain (FDTD) was performed to optimize the geometric parameters of SRR to make the magnetic dipole resonance wavelength around 1550 nm (the center wavelength of femtosecond laser). The nonlinear conversion efficiency of SRRs strongly depends on the excitation of local Plasmon resonance. For the first-order dip of transmission spectrum, the electric field can couple to the capacitance of the SRR and induce a circulating current in the coil leading to a magnetic dipole moment normal to the SRR plane.^[45] This magnetic response, which is associated with the Lorenz force, brings the resonant enhancement of the local magnetic field.^[46] Due to the co-existence of resonance and local field enhancement, the nonlinear responses of SRRs are significantly improved. However, if the resonance wavelength deviates from the 1550 nm, the magnetic dipole resonance will weaken or disappear, the nonlinear

signal will be very weak, which is detrimental to the realization of the multiplexed metasurface we designed. The SRR is placed on fused silica substrate, with 350 nm period in x and y directions. In the numerical simulations, a meta-atom is chosen as the simulated structure with periodic boundary conditions at x and y directions and perfectly matched layers along the z direction. The meta-atom is illuminated vertically with plane waves in the direction of substrate. The optimized SRR has a length of 168 nm, a width of 150 nm, a height of 35 nm, and an arm width of 40 nm. The simulated linear transmission spectra for horizontal and vertical polarized incident lights of the regularly arranged SRRs are shown in Figure 1b. According to the simulated transmission spectra, the resonance dip is around the wavelength of 1550 nm, which results from the magnetic-dipole mode of SRRs. So the strongest nonlinear response can be expected for FF around the resonance wavelength of 1550 nm. The experimentally measured transmission spectra were acquired by a Bruker VERTEX 70 Fourier-transform infrared spectrometer, as shown in Figure 1c. The noise of measured transmission spectra is caused by the truth that the position of short wavelength is near and a little below the detection spectral range of the instrument, yet we can still get the information of resonance wavelengths of SRRs from the measured transmission spectra. The slight differences of resonance wavelengths between the experimentally measured and simulated results may be induced by fabrication imperfections. The inset of Figure 1c shows the scanning electron microscopy (SEM) image of the sample with regularly arranged gold SRRs.

Using two rules mentioned above and the SRRs with defined parameters, we designed the multifocal metalens and

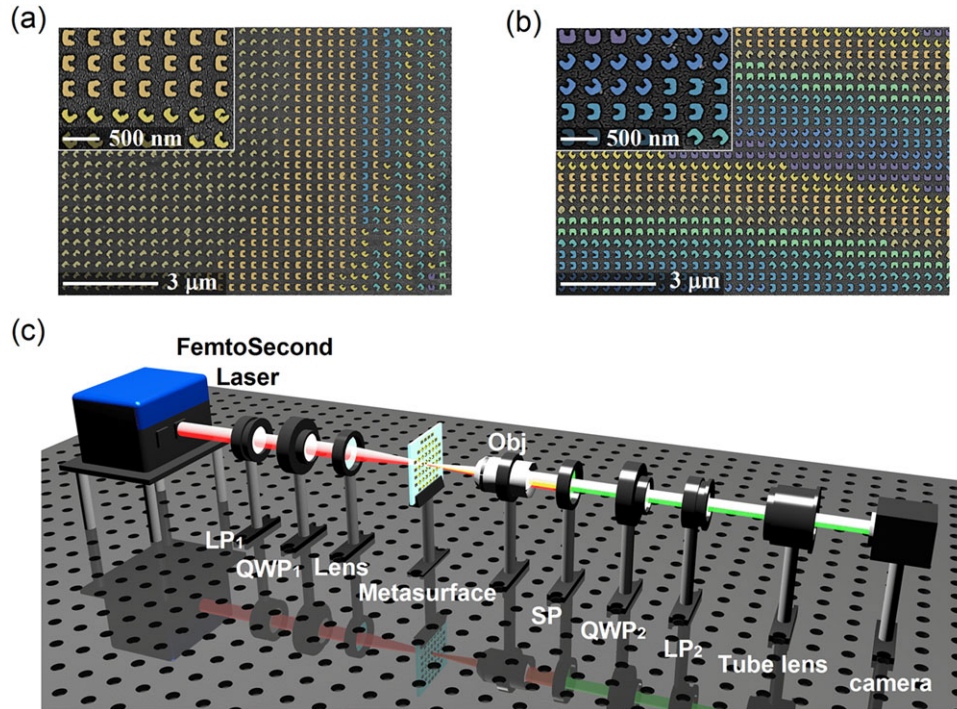


Figure 2. An SEM image of the fabricated metasurfaces and experimental setup. a) SEM image of the fabricated metalens with low and high magnifications. Different colors represent meta-atoms with distinctive orientation angles. b) SEM images of the multifunctional metasurface with low and high magnifications. c) Schematic of experiment setup for linear and nonlinear signal measurements. A linear polarizer and a quarter-wave plate are used to generate a circular polarized beam, which is focused onto the sample by a lens. An objective is used to enlarge the image, followed by a short- or long-pass filter to block the fundamental wave or second harmonic wave. Then another set of a QWP₂ and an LP₂ is used to ensure that only the signal with certain circular polarization state will be measured and then collected with a tube lens and a scientific camera.

multifunctional metasurface to verify the effectiveness of nonlinear coding metasurfaces. Two samples were fabricated by standard electron-beam lithography (EBL) and lift-off procedure (see Methods for details). **Figure 2a,b** shows the SEM images of the metalens and the multifunctional metasurface, respectively, in which the different colors of SRRs represent distinctive orientation angles of meta-atoms. The various focusing functionalities and images information generated by the designed samples can be captured and read by selecting certain channels in our experimental setup, which is schematically shown in **Figure 2c**.

By applying linear and nonlinear coding elements, we realized an ultrathin flat metalens with different focal lengths under different channels (THG, FF, and SHG). **Figure 3a–c** schematically shows the focusing processes and distributions of digital elements of multifocal metalens under different channels. According to the first rule mentioned above, the metalens excited by an LCP fundamental wave has three different phase distributions (4φ , 2φ , and φ) under the three channels (THG, FF, and SHG), which represent three different coding patterns. To achieve the function of focusing by the Fresnel zone plate composed of discrete phases, the optical path difference between two adjacent coding zones needs to satisfy:

$$\sqrt{r_{i+1}^2 + f^2} - \sqrt{r_i^2 + f^2} = \frac{\lambda}{N} \quad (1)$$

where f is the focal length, r_i ($i = 1, 2, 3, \dots$) is the outer radius of zone i , $\sqrt{r_i^2 + f^2}$ stands for the optical path from zone i to the focal point, and N represents the quantization order of the phases. The quantization order N is equal to 2, 4, and 8 under the channel of THG, FF, and SHG, respectively, which stands for the number of discrete phases in different channels. In the paraxial approximation, by applying a Taylor series $(1+x)^n \approx 1+nx$ to the first order, Equation (1) can be approximated as $r_{i+1}^2 - r_i^2 \approx 2\lambda f/N$. For the three channels, the wavelengths satisfy $3\lambda_{\text{THG}} = \lambda_{\text{FF}} = 2\lambda_{\text{SHG}}$ and the quantization orders satisfy the relation $4N_{\text{THG}} = 2N_{\text{FF}} = N_{\text{SHG}}$. According to the approximate formula $r_{i+1}^2 - r_i^2 \approx 2\lambda f/N$, it is easy to obtain this relation $f_{\text{THG}} \approx 3f_{\text{FF}}/2 \approx 3f_{\text{SHG}}/8$. That is to say, under the paraxial approximation, if a metalens can focus the THG, it can certainly focus both the FF and the SHG, which is consistent with the conclusion deduced from the continuous phase distribution of lens.

The process of 1-bit digital coding is first implemented to design the ultrathin multifocal metalens under the channel of THG. By utilizing the coding elements of this channel, a nonlinear binary-phase Fresnel zone plate can be programmed as follows. According to Equation (1), to obtain constructive interference at the focal point, the optical path difference between two adjacent coding zones needs to satisfy:

$$\sqrt{r_{i+1}^2 + f_{\text{THG}}^2} - \sqrt{r_i^2 + f_{\text{THG}}^2} = \frac{\lambda_{\text{THG}}}{2} \quad (2)$$

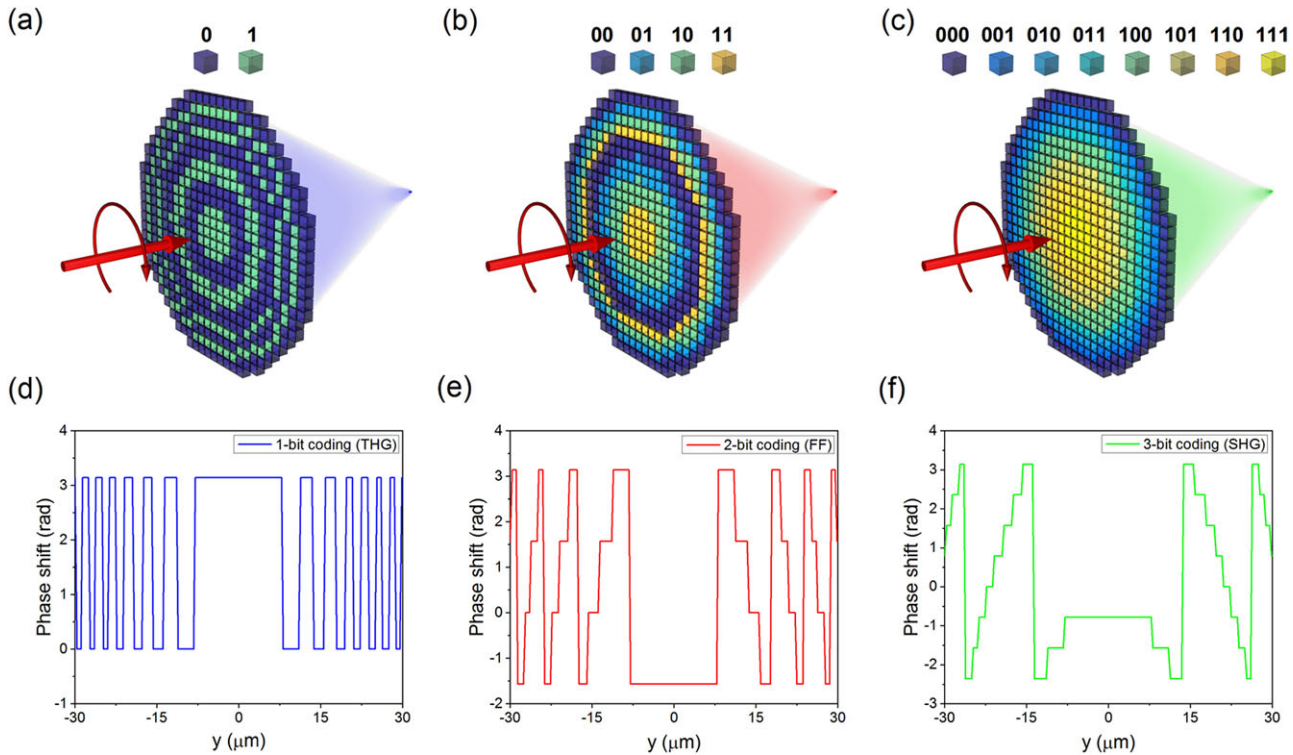


Figure 3. Schematic drawings and phase distributions of the designed multifocal metalens under different channels. a–c) The focusing procedures of the same coding metalens under the THG (a), FF (b), and SHG (c) channels. Only the schematic distributions of digital elements are shown on the sample surfaces. d–f) The spatial radial distributions of P–B phases of the metalens for the THG (d), FF (e), and SHG (f) channels within the diameter of 60 μm , taking the center of the metalens as the origin.

So we can achieve that the outer radius of $(i + 1)$ th zone should satisfy $r_{i+1} = \sqrt{(\sqrt{r_i^2 + f_{\text{THG}}^2} + \lambda_{\text{THG}}/2)^2 - f_{\text{THG}}^2}$. Then, we constructed the nonlinear binary-phase Fresnel zone plate with $r_1 = 8 \mu\text{m}$ and $f_{\text{THG}} = 120 \mu\text{m}$ for THG. The coding sequences, consist of the digital element of each zone starting from the center of plate, are 1–0–1–0–1–0–1–0–1... (Figure 3a). From the relations of coding elements outlined in Table 1, the coding sequences of this Fresnel zone plate for the FF channel are 11–10–01–00–11–10–01–00–11... (Figure 3b), and the coding sequences for the channel of SHG are 111–110–101–100–011–010–001–000–111... (Figure 3c). Based on the spatial coding distribution of the Fresnel zone plate and the relations between the digital elements and the P–B phases, the spatial radial distributions of P–B phases for the three channels can be achieved, as shown in Figure 3d–f. In order to more clearly show their characteristics, we only display the phase distributions within the diameter of 60 μm . The metalens with diameter of 200 μm was fabricated in terms of the nonlinear P–B phase distribution of SHG.

To confirm the multiplexed performance of the metalens with different focal lengths under different channels, we numerically calculated its far-field distributions under three different channels by using the Fresnel–Kirchhoff diffraction formula, as shown in Figure 4a–c. We calculated the intensity profiles of different channels behind the metalens in the y – z cross section, taking the center of the metalens as the origin. From the calculated results, we can find that the wave front of the transmitted beam for each channel can be converged simultaneously. Perfect

focusing for the THG channel is achieved with the focal length of 120 μm (Figure 4a). The foci of the FF and SHG channels are extended to the line shape (Figure 4b,c). In particular, the expansion for the FF channel is even more pronounced, which covers the range of $z = 50$ – $80 \mu\text{m}$. This phenomenon can be attributed to two intrinsic reasons. First, according to the focusing theory mentioned above, perfect focusing of the metalens in the FF and SHG channels can be achieved when the approximate condition $r \ll f$ is satisfied, yet the metalens we designed has the diameter of 200 μm , which does not meet the paraxial approximation. Actually, the sample with smaller diameter will be expected to achieve more excellent focusing performances for the FF and SHG (see Figure S1, Supporting Information). Second, the difference between the phase distribution of the multifocal metalens and the ideal hyperboloidal phase distribution also contributes to the expansion of foci.

For an LCP incident fundamental beam, the intensity profiles of different channels behind the metalens were experimentally measured, as shown in Figure 4d–f, which are in good agreement with the calculated results validating the multifocal metalens as a viable method for achieving simultaneous focusing under the three different channels. The focal lengths for different channels $f_{\text{THG}} = 127 \mu\text{m}$, $f_{\text{FF}} = 68 \mu\text{m}$, and $f_{\text{SHG}} = 399 \mu\text{m}$ can be obtained by experimental results. According to the definition of numerical aperture $\text{NA} = n \cdot \sin[\arctan(D/2f)]$, we can also obtain the numerical apertures of the designed metalens, which are 0.640, 0.781, and 0.298 for the THG, FF, and SHG channels,

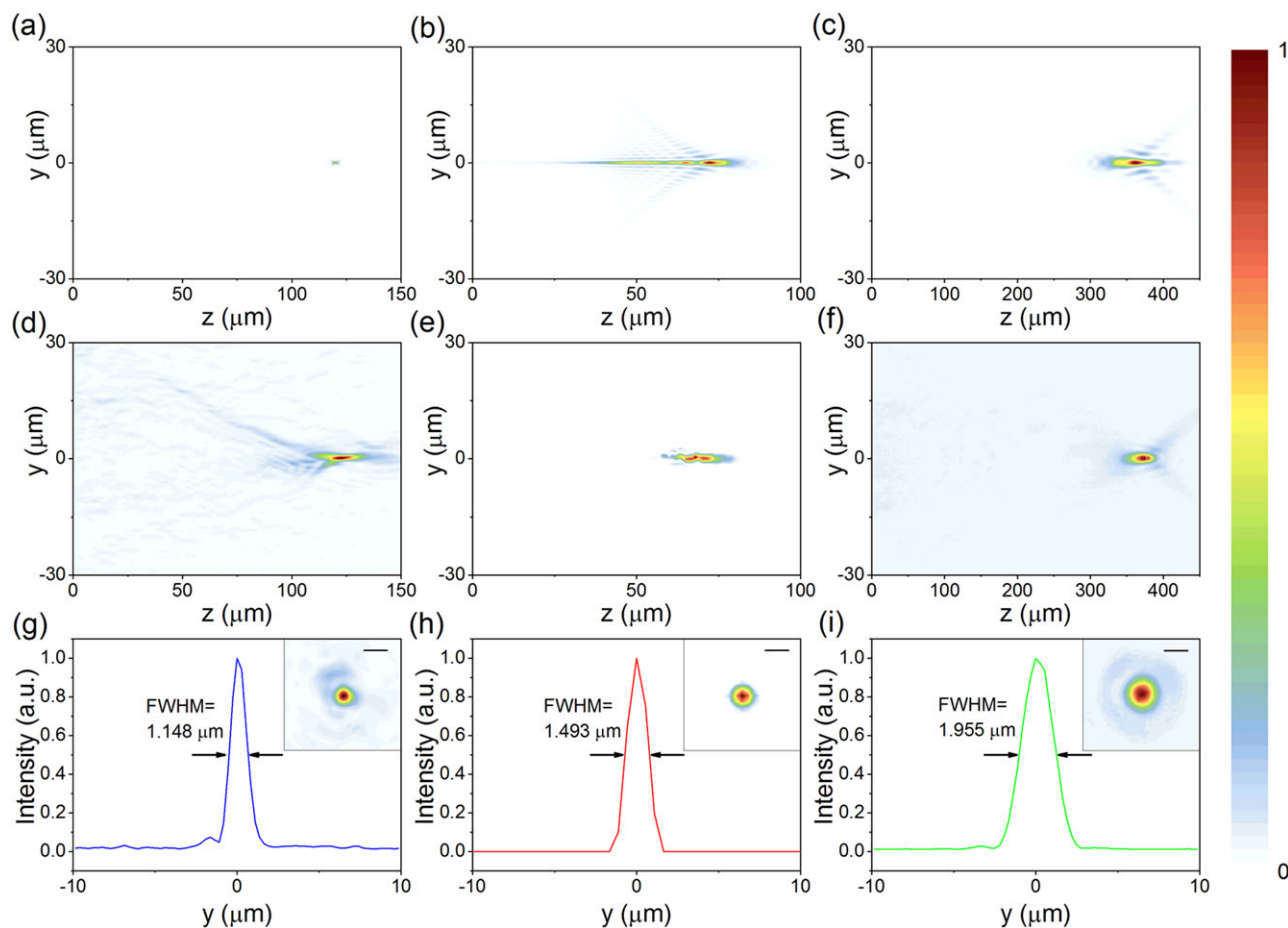


Figure 4. Calculated and experimental intensity profiles of the metalens. a–c) Numerically calculated intensity profiles for THG (a), FF (b), and SHG (c) in the y - z plane. d–f) Experimentally measured intensity distributions for THG (d), FF (e), and SHG (f) in the y - z cross section. The center of the metalens is taken as the origin in (a–f). g–i) The experimentally measured intensity distributions of the focal spots along y -axis for THG (g), FF (h), and SHG (i). The insets in (g–i) represent the measured intensity profiles of x - y cross sections at the focal planes (scale bar: $2\ \mu\text{m}$).

respectively. Figure 4g–i shows the experimentally measured intensity distributions of THG, FF, and SHG along y -axis at the foci, respectively. The insets represent the measured intensity profiles of x - y cross section at the focal plane. The NAs of the objectives used in the linear and nonlinear measurement are 0.67 and 0.45, respectively, which are smaller than those of the metalens under the channels of FF and THG. Although this may reduce the intensity and resolution of the metalens at the focal point, the measured functionalities and focal length remain correct. The metalens that can simultaneously achieve focusing under the channels of SHG, THG, and FF is demonstrated.

The nonlinear coding multifunctional metasurface can be further constructed by using the extra degree of freedom mentioned in the second rule. As shown in Figure 5a–c, the function of focusing, operational symbols “+” and “–,” are encoded in the channels of THG, FF, and SHG, respectively. We first design the multifunctional metasurface to focus the wave front of THG at the focal length of $120\ \mu\text{m}$. Therefore, under the THG channel, a nonlinear binary-phase Fresnel zone plate is programmed in the same way as the multifocal metalens designed before (Figure 5a). According to the extra degree of freedom mentioned above, when

the coding elements of the THG channel in a certain zone are all “1,” the coding elements can be “01” or “11” under the channel of FF. Therefore, on the basis of maintaining the coding array of THG channel unchanged, the FF signal can achieve destructive interference (01–11, phase mismatching) or constructive interference (01–01 or 11–11, phase matching) in the far field. So, the operational symbols “+” can be stored in the FF channel utilizing the real space image coding (Figure 5b). Similarly, when the coding elements in the FF channel are “01,” the digital elements can be “001” or “101” under the channel of SHG. The operational symbols “–” can be stored in the channel of SHG in the same way (Figure 5c). It is worth noting that to achieve perfect destructive interference, a large phase gradient on the metasurface is required, which corresponds to high spatial frequencies ($\nu_x^2 + \nu_y^2 > \lambda^{-2}$, where ν_x and ν_y represent the spatial frequencies of the metasurface in x and y directions, respectively).^[47] In this case, the output wave will be converted into evanescent wave and vanish in the far field. Therefore, a period of $350\ \text{nm}$ is selected to meet this condition. For consistency, the sample consisting of regularly arranged gold SRRs and the multifocal metalens mentioned above also have the same period of $350\ \text{nm}$.

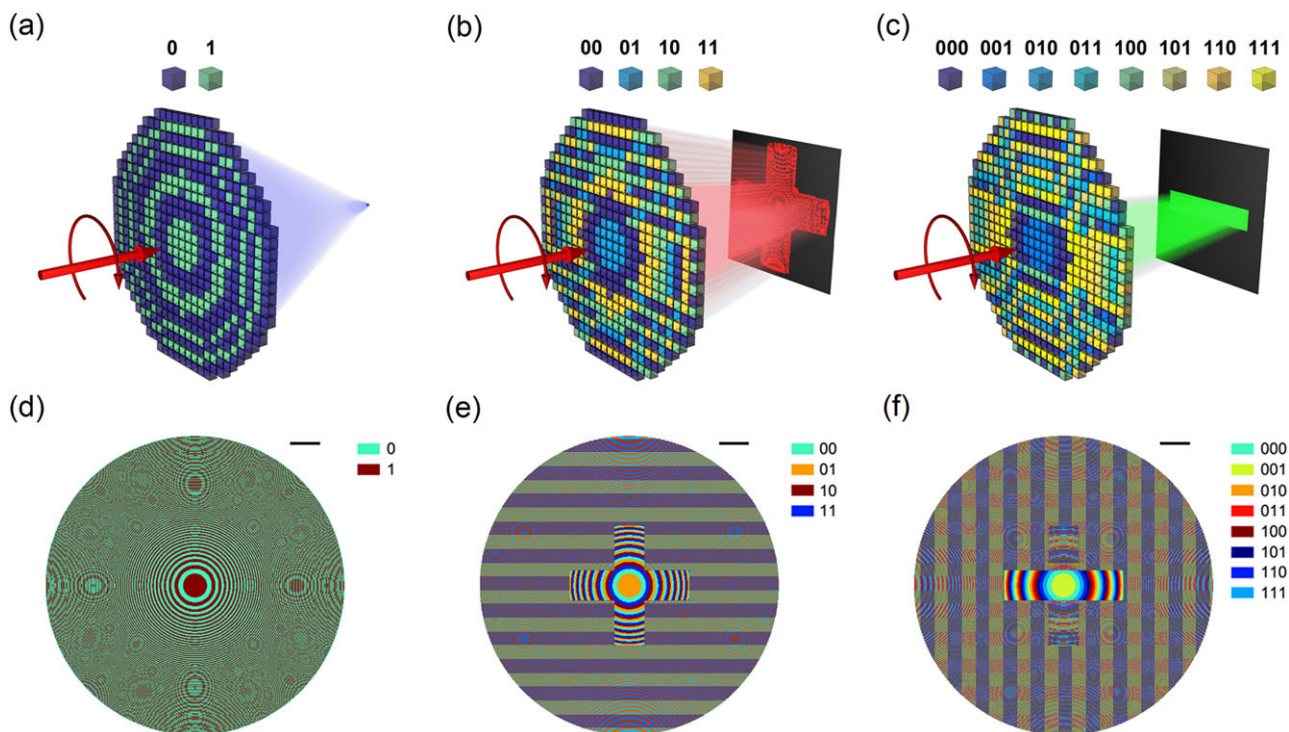


Figure 5. Schematic diagrams and coding patterns of the designed multifunctional metasurface. a) The focusing procedure for the THG channel. b,c) The reconstruction procedures of the operational symbols “+” of the FF channel (b) and “−” of the SHG channel (c). Only the schematic distributions of digital elements are shown on the sample surfaces in (a–c). d–f) The coding patterns of multifunctional metasurface for the THG (d), FF (e), and SHG (f). The scale bars represent 20 μm .

The coding patterns for different channels are shown in Figure 5d–f, which are designed to obtain the function of focusing, operational symbols “+” and “−” under the THG, FF, and SHG channels, respectively (see Figure S2, Supporting Information, for further details). To demonstrate the feasibility of the nonlinear coding multifunctional metasurface, we numerically calculated the far-field distributions under the three channels (Figure 6a–c) and performed proof-of-concept experiments (Figure 6d–f). As observed, the wave front of the THG is converged well in the results of numerical calculation (Figure 6a) and experiment (Figure 6d), and the symbol “+” is perfectly reproduced by numerical calculation (Figure 6b) and experiment (Figure 6e) under the FF channel. Due to the limitation of the nonlinear conversion efficiency of SRRs, the intensity of the desired symbol “−” produced by the constructive interference among neighboring meta-atoms is relatively weak, we therefore calculated and measured the profile of the symbol “−” being focused in the relatively far field (Figure 6c,f). The focused symbol “−” is consistently demonstrated by the calculated and experimental results, which confirms the validity of the design concept of the nonlinear coding multifunctional metasurface. It is desired to achieve a more pronounced image of symbol “−” in the far field when the SHG from the SRR has a higher intensity. Besides, in order to further verify the feasibility of optical information multiplexing in nonlinear coding metasurfaces, we theoretically designed the nonlinear coding metasurface which stores different information in different channels, and ensures the information remains relatively independent of each other (see Figure S3, Supporting Information).

From the numerically calculated results of this nonlinear coding metasurface, the intensity profiles in the far field are highly consistent with the multiplexed functionality we designed, which confirms it is viable to implement multi-channel optical information storage by exploiting nonlinear coding metasurfaces.

3. Conclusions and Outlook

In conclusion, benefitting from the unique properties of the linear and nonlinear P–B phases, we proposed a strategy to design the metasurfaces with multiplexed functionality, which combines the convenient DSP in coding and the multidimensional information channels in nonlinear optical processes. To confirm the feasibility and flexibility of this methodology, we theoretically designed and experimentally demonstrated the nonlinear coding metalens, which can simultaneously achieve the desired focusing functionalities at the three channels. Furthermore, by utilizing the extra degree of freedom among the coding elements of the three channels, the multifunctional metasurface which encoded different information into different channels was presented and experimentally verified. The proposed design method allows flexible and convenient manipulation for the wave front of each channel while ensuring the relative independence among the three channels, which provides a new strategy for information multiplexing. With the rapid development of nonlinear material systems with enhanced conversion efficiency, the nonlinear coding metasurfaces may provide a promising platform for optical

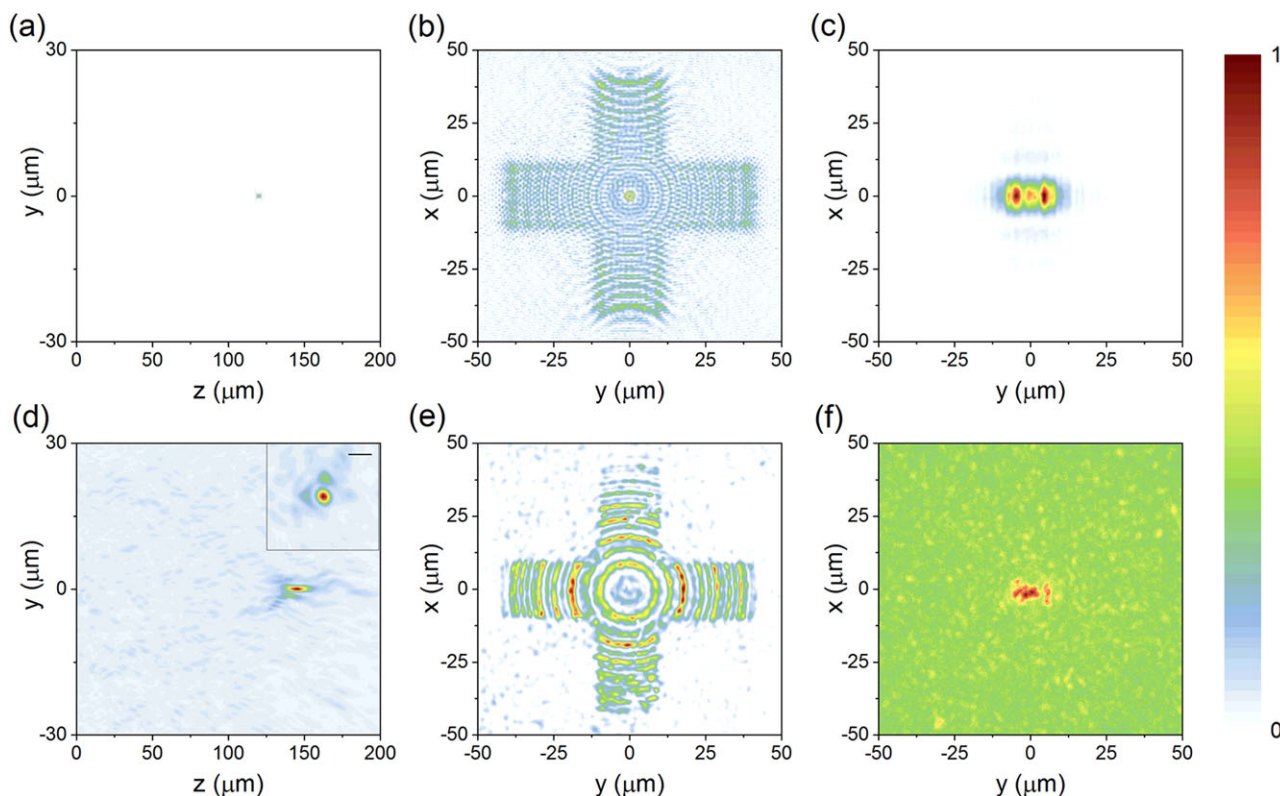


Figure 6. Calculated and experimental intensity profiles of the nonlinear coding multifunctional metasurface. a) Calculated intensity profile for THG in the y - z plane. b) Numerically calculated real space image under the FF channel. A perfect symbol “+” is obtained in the far field. c) Numerically calculated image under the SHG channel. A focused symbol “-” is achieved in the relatively far field. (b) and (c) show the calculated real space images in the x - y plane. d-f) Measured results corresponding to (a-c) for the multifunctional metasurface. The inset in (d) represents the measured intensity distribution of focal spot at the focal plane (scale bar: 2 μm).

encryption, information multiplexing, multi-channel optical data storage, and real space encoding imaging.

4. Experimental Section

Sample Fabrication: The metasurface was fabricated on the fused silica substrate with standard EBL and lift-off procedure. First, the fused silica substrate were spun coated with a layer of poly(methyl methacrylate) (PMMA) with thickness of 120 nm. Then to eliminate the charging effect on the dielectric substrate during the EBL process which employing a 100 kV voltage, 200 pA current and 1000 $\mu\text{C cm}^{-2}$ dose, a layer of poly(3,4-ethylenedioxythiophene) polystyrene sulfonate (PEDOT:PSS) with thickness of 35 nm were spun-coated. After defining the patterns of designed SRRs arrays by the EBL process, the PEDOT:PSS layer was removed with pure water for 60 s and PMMA was developed with methyl isobutyl ketone (MIBK)/isopropyl alcohol (IPA) (3:1) for 40 s. After that, a 2 nm Cr adhesion layer and a 35 nm thick gold layer were deposited on the resist by sequence utilizing electron beam evaporation deposition (EBD). During the final lift-off procedure, the Cr film was striped by removing PMMA with hot acetone at degree of 60 °C for 20 min, remaining the SRRs arrays on the substrate.

Measurement Procedure: An erbium-doped ultrafast fiber laser (Toptica Photonics AG FemtoFiber Pro NIR, repetition frequency: 80 MHz, pulse length: ≈ 80 fs) centered at 1550 nm was used as fundamental beam source. Both linear and nonlinear signals were measured by coupling the beam source to a home-built microscope. The combination of an LP₁ and a QWP₁ was used to convert the incident beam into LCP light. Then the light was normally incident on the metasurface and the emitted linear and

nonlinear signals in transmission direction were filtered by another set of QWP₂ and an LP₂ to ensure that only the signal with certain circular polarization state was measured, then collected with an objective, a tube lens and a scientific camera. The objective, tube lens (Thorlabs ITL200), and camera were all integrated on a three-axis motorized translation stage to measure the focusing profiles and capture the real space image of emitted signals with a step of 1 μm along z -axis. For linear measurement, the average power of the excitation beam was set to 1 mW, and the output light from the metasurface is collected with a 50 \times objective (SIGMA-KOKI PAL-50-NIR-HR-LC00 50 \times NA = 0.67) and an InGaAs camera (HAMAMATSU InGaAs C10633), the lens and short-pass filter are removed. For nonlinear measurement, a lens ($f = 150$ mm) was used to focus the fundamental pulses with an average power of 350 mW to a spot size diameter of ≈ 200 μm , which corresponds to a peak intensity of 0.17 GW cm^{-2} . Then the SHG and THG signals were captured by a 20 \times objective (SIGMA-KOKI PAL-20-NIR-HR-LC00 20 \times NA = 0.45) and an CMOS camera (HAMAMATSU ORCA-Flash4.0 V3). For the measurement of THG signal, a long-pass filter is placed after the short-pass filter to block the second harmonic.

Supporting Information

Supporting Information is available from the Wiley Online Library or from the author.

Acknowledgements

This work was supported by the National Key Research and Development Program of China (2016YFA0301102 and 2017YFA0303800), the

Ministry of Science and Technology of China (2016YFA0200803 and 2016YFA0200402), the National Natural Science Foundation of China (91856101, 11774186 and 11574163), Natural Science Foundation of Tianjin for Distinguished Young Scientists (18JCJC45700), the Natural Science Foundation of Tianjin (16JCQNJC01700), and 111 Project (B07013).

Conflict of Interest

The authors declare no conflict of interest.

Keywords

digital signal processing, multiplexing, nonlinear coding metasurfaces, Pancharatnam–Berry phase, real space imaging

Received: February 10, 2019

Revised: April 11, 2019

Published online:

- [1] J. Valentine, S. Zhang, T. Zentgraf, E. Ulin-Avila, D. A. Genov, G. Bartal, X. Zhang, *Nature* **2008**, 455, 376.
- [2] D. R. Smith, W. J. Padilla, D. Vier, S. C. Nemat-Nasser, S. Schultz, *Phys. Rev. Lett.* **2000**, 84, 4184.
- [3] J. Pendry, *Science* **2004**, 306, 1353.
- [4] S. Zhang, Y. S. Park, J. Li, X. Lu, W. Zhang, X. Zhang, *Phys. Rev. Lett.* **2009**, 102, 023901.
- [5] M. Khorasaninejad, W. T. Chen, R. C. Devlin, J. Oh, A. Y. Zhu, F. Capasso, *Science* **2016**, 352, 1190.
- [6] J. Pendry, *Science* **2008**, 322, 71.
- [7] N. Fang, H. Lee, C. Sun, X. Zhang, *Science* **2005**, 308, 534.
- [8] J. B. Pendry, D. Schurig, D. R. Smith, *Science* **2006**, 312, 1780.
- [9] J. Valentine, J. Li, T. Zentgraf, G. Bartal, X. Zhang, *Nat. Mater.* **2009**, 8, 568.
- [10] J. Li, J. B. Pendry, *Phys. Rev. Lett.* **2008**, 101, 203901.
- [11] B. Edwards, A. Alu, M. G. Silveirinha, N. Engheta, *Phys. Rev. Lett.* **2009**, 103, 153901.
- [12] L. Huang, X. Chen, H. Mühlenbernd, H. Zhang, S. Chen, B. Bai, Q. Tan, G. Jin, K.-W. Cheah, C.-W. Qiu, J. Li, T. Zentgraf, S. Zhang, *Nat. Commun.* **2013**, 4, 2808.
- [13] X. Ni, A. V. Kildishev, V. M. Shalaev, *Nat. Commun.* **2013**, 4, 2807.
- [14] S. Larouche, Y. J. Tsai, T. Tyler, N. M. Jokerst, D. R. Smith, *Nat. Mater.* **2012**, 11, 450.
- [15] E. Almeida, O. Bitton, Y. Prior, *Nat. Commun.* **2016**, 7, 12533.
- [16] W. Liu, Z. Li, H. Cheng, C. Tang, J. Li, S. Zhang, S. Chen, J. Tian, *Adv. Mater.* **2018**, 30, 1706368.
- [17] N. Yu, P. Genevet, M. A. Kats, F. Aieta, J.-P. Tetienne, F. Capasso, Z. Gaburro, *Science* **2011**, 334, 333.
- [18] S. Sun, K. Y. Yang, C. M. Wang, T. K. Juan, W. T. Chen, C. Y. Liao, Q. He, S. Xiao, W. T. Kung, G. Y. Guo, L. Zhou, D. P. Tsai, *Nano Lett.* **2012**, 12, 6223.
- [19] X. Ni, N. K. Emani, A. V. Kildishev, A. Boltasseva, V. M. Shalaev, *Science* **2012**, 335, 427.
- [20] F. Aieta, P. Genevet, N. Yu, M. A. Kats, Z. Gaburro, F. Capasso, *Nano Lett.* **2012**, 12, 1702.
- [21] Z. Liu, Z. Li, Z. Liu, J. Li, H. Cheng, P. Yu, W. Liu, C. Tang, C. Gu, J. Li, S. Chen, J. Tian, *Adv. Funct. Mater.* **2015**, 25, 5428.
- [22] H. Cheng, S. Chen, P. Yu, W. Liu, Z. Li, J. Li, B. Xie, J. Tian, *Adv. Opt. Mater.* **2015**, 3, 1744.
- [23] C. Wang, W. Liu, Z. Li, H. Cheng, Z. Li, S. Chen, J. Tian, *Adv. Opt. Mater.* **2018**, 6, 1701047.
- [24] L. Huang, X. Chen, H. Mühlenbernd, G. Li, B. Bai, Q. Tan, G. Jin, T. Zentgraf, S. Zhang, *Nano Lett.* **2012**, 12, 5750.
- [25] P. Genevet, J. Lin, M. A. Kats, F. Capasso, *Nat. Commun.* **2012**, 3, 1278.
- [26] P. Genevet, N. Yu, F. Aieta, J. Lin, M. A. Kats, R. Blanchard, M. O. Scully, Z. Gaburro, F. Capasso, *Appl. Phys. Lett.* **2012**, 100, 013101.
- [27] J. Li, S. Chen, H. Yang, J. Li, P. Yu, H. Cheng, C. Gu, H.-T. Chen, J. Tian, *Adv. Funct. Mater.* **2015**, 25, 704.
- [28] X. Yin, Z. Ye, J. Rho, Y. Wang, X. Zhang, *Science* **2013**, 339, 1405.
- [29] Z. Li, W. Liu, H. Cheng, S. Chen, J. Tian, *Adv. Opt. Mater.* **2017**, 5, 1700413.
- [30] N. Shitrit, I. Bretner, Y. Gorodetski, V. Kleiner, E. Hasman, *Nano Lett.* **2011**, 11, 2038.
- [31] X. Ling, X. Zhou, X. Yi, W. Shu, Y. Liu, S. Chen, H. Luo, S. Wen, D. Fan, *Light: Sci. Appl.* **2015**, 4, e290.
- [32] J. Zhou, H. Qian, G. Hu, H. Luo, S. Wen, Z. Liu, *ACS Nano* **2018**, 12, 82.
- [33] T. J. Cui, M. Q. Qi, X. Wan, J. Zhao, Q. Cheng, *Light: Sci. Appl.* **2014**, 3, e218.
- [34] C. Della Giovampaola, N. Engheta, *Nat. Mater.* **2014**, 13, 1115.
- [35] L.-H. Gao, Q. Cheng, J. Yang, S.-J. Ma, J. Zhao, S. Liu, H.-B. Chen, Q. He, W.-X. Jiang, H.-F. Ma, Q.-Y. Wen, L.-J. Liang, B.-B. Jin, W.-W. Liu, L. Zhou, J.-Q. Yao, P.-H. Wu, T.-J. Cui, *Light: Sci. Appl.* **2015**, 4, e324.
- [36] S. Liu, A. Noor, L. L. Du, L. Zhang, Q. Xu, K. Luan, T. Q. Wang, Z. Tian, W. X. Tang, J. G. Han, W. L. Zhang, X. Y. Zhou, Q. Cheng, T. J. Cui, *ACS Photonics* **2016**, 3, 1968.
- [37] S. Liu, T. J. Cui, Q. Xu, D. Bao, L. Du, X. Wan, W. X. Tang, C. Ouyang, X. Y. Zhou, H. Yuan, H. F. Ma, W. X. Jiang, J. Han, W. Zhang, Q. Cheng, *Light: Sci. Appl.* **2016**, 5, e16076.
- [38] B. Xie, K. Tang, H. Cheng, Z. Liu, S. Chen, J. Tian, *Adv. Mater.* **2017**, 29, 1603507.
- [39] B. Xie, H. Cheng, K. Tang, Z. Liu, S. Chen, J. Tian, *Phys. Rev. Appl.* **2017**, 7, 024010.
- [40] J.-P. Xia, D. Jia, H.-X. Sun, S.-Q. Yuan, Y. Ge, Q.-R. Si, X.-J. Liu, *Adv. Mater.* **2018**, 30, 1805002.
- [41] W. Ye, F. Zeuner, X. Li, B. Reineke, S. He, C. W. Qiu, J. Liu, Y. Wang, S. Zhang, T. Zentgraf, *Nat. Commun.* **2016**, 7, 11930.
- [42] F. Walter, G. Li, C. Meier, S. Zhang, T. Zentgraf, *Nano Lett.* **2017**, 17, 3171.
- [43] Z. Li, W. Liu, Z. Li, C. Tang, H. Cheng, J. Li, X. Chen, S. Chen, J. Tian, *Laser Photonics Rev.* **2018**, 12, 1800164.
- [44] G. Li, S. Chen, N. Pholchai, B. Reineke, P. W. Wong, E. Y. Pun, K. W. Cheah, T. Zentgraf, S. Zhang, *Nat. Mater.* **2015**, 14, 607.
- [45] C. Enkrich, M. Wegener, S. Linden, S. Burger, L. Zschiedrich, F. Schmidt, J. Zhou, T. Koschny, C. Soukoulis, *Phys. Rev. Lett.* **2005**, 95, 203901.
- [46] M. W. Klein, C. Enkrich, M. Wegener, S. Linden, *Science* **2006**, 313, 502.
- [47] J. Li, P. Yu, C. Tang, H. Cheng, J. Li, S. Chen, J. Tian, *Adv. Opt. Mater.* **2017**, 5, 1700152.